Microsc. Microanal., page 1 of 9
doi:10.1017/S1431927614000956

Microscopy and Microanalysis

Analytical Formulae for Calculation of X-Ray Detector Solid Angles in the Scanning and Scanning/Transmission Analytical Electron Microscope

Nestor J. Zaluzec*

Argonne National Laboratory, Electron Microscopy Center, Argonne, IL 60440, USA

Abstract: Closed form analytical equations used to calculate the collection solid angle of six common geometries of solid-state X-ray detectors in scanning and scanning/transmission analytical electron microscopy are presented. Using these formulae one can make realistic comparisons of the merits of the different detector geometries in modern electron column instruments. This work updates earlier formulations and adds new detector configurations.

Key words: solid angle, XEDS, microanalysis, STEM, TEM, SEM, SDD, SiLi, X-ray detectors, EDS, EDXS

Introduction

An important figure of merit used to assess the relative collection efficiency of an X-ray energy dispersive spectrometer (XEDS) interfaced to an electron optical column is its associated collection solid angle (Ω). This parameter describes the angular extent of signal emitted by a point source and collected by the detector system. The ideal detector would completely surround an isotropically emitting point source and have a collection solid angle of 4π steradians. Due to the practical constraints of specimen shape and support, instrumentation access, as well as the physical geometry of interfacing a detector to an analytical microscope reaching this level of collection efficiency (i.e., $4\pi = 100\%$), is unrealizable. Nevertheless, the specification and use of collection solid angle as a qualifying parameter which can be used to assess the advantages of a detector configuration, rather than its physical size, is an important distinction. This is most important when assessing various geometries as physically larger detectors do not always correlate with greater collection solid angles and thus more efficient and statistically significant data collection or greater sensitivity capabilities (Zaluzec, 2013*a*).

For the first 3 decades of their use the geometry of solid state X-ray detectors in electron-optical instruments remained virtually stagnant, with cylindrical shaped devices of lithium drifted silicon (Si(Li)) or high purity germanium being the norm (Fitzgerald *et al.*, 1968; Knoll, 1999). During the last decade the advent and commercial availability of silicon drift detectors (SDD), which can be fabricated into a variety of shapes and sizes, have dramatically transformed our capabilities to introduce novel and versatile detectors in today's instruments (Gatti, 1984). Along with their ability of increased processing speed and data throughput, customized geometries with physically large areas are now realizable (Iwanczyk *et al.*, 2005; Soltau *et al.*, 2009; Zaluzec, 2009; PN Detector, 2013; Ketek, 2013). Because of the versatile configurations which can be enabled with SDD technology, it becomes important to correctly assess their signal collection abilities, particularly in light of the fact that these detectors are being pressed into service in ever increasing roles where sensitivity and signal collection are of utmost importance.

In an earlier study (Zaluzec, 2009), formulations for two geometries were analyzed and closed form solutions for calculating the solid angle of detectors developed. In this work, we update that previous analysis and add a compendium of new variations, which are now commercially available.

Ideally, experimental determination of an important parameter such as Ω would be preferred over a theoretical calculation when accurate comparisons or assessments of the relative efficiency of detectors are to be conducted. Unfortunately, these are tedious measurements, and as such are seldom performed in the laboratory (Watanabe and Wade, 2013; Zaluzec, 2013*a*). Three dimensional modeling using computer aided drawing programs is an alternative used by some manufacturers, however, the access to such capability is generally not available to the community at large. Analytical formulations therefore serve as a valuable assessment methodology, allowing individual researcher's to explore parameter space so as to make logical and informed decisions on the viability of an experiment or configuration.

Formulation and Discussion

We begin by recalling that the subtending/collection solid angle (Ω) of a detector relative to a point source is the areal projection (S) of the detector shape viewed from that point onto the surface of a bounding sphere of radius R that completely encloses the detector *active* area (Fig. 1). For this

Received January 1, 2014; accepted April 22, 2014
**Corresponding author*. Zaluzec@aaem.amc.anl.gov

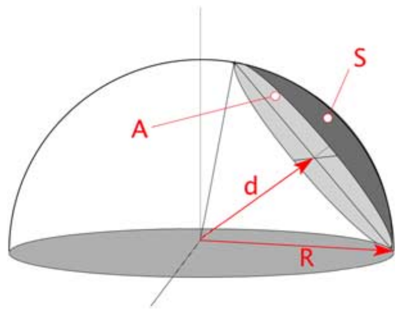

Figure 1. Conventional X-ray detector solid angle, defined as the projected surface area (S) of a detector area (A) at a distance (d) from the region of interest onto a bounding sphere of radius (R).

configuration the collection solid angle is given exactly by the equation:

$$\Omega = \frac{S}{R^2} \tag{1}$$

As highlighted in the previous study, the most common error used in the application of this equation is the frequently employed approximation which equates S with the *total* detector area (A) and R with its radial distance (d) from the source point to the surface of the detector (Fig. 2a). In the electron microscope, for large values of "d" (i.e., $\geq$15 mm) and small values of "A" ($\leq$30 mm^2), the approximation is reasonable, however outside of these limits significant errors can be introduced.

Calculation of the projected surface area (S) for an arbitrary shaped detector is a detailed task. Fortunately, a significant simplification exists owing to the fact that the active surface of today's X-ray detectors are generally planar sections whose projection upon a sphere can be mathematically described. For regular planar shapes (circles, cylinders, annuli, arcs, squares, rectangles) we can derive closed form analytical solutions of the projected surface area, so long as the surface normal of the detector plane is a radial vector to the specimen (i.e., the plane of the detector is tangential to a sphere centered at the point of interest on the specimen). We will consider non-radial detectors (i.e., a non-tangential detector geometry) as a special case later in this paper.

Circular and Cylindrical Detectors

In this geometry one can describe the detector as a right circular cylinder, having an active area radius (r_a), and located a radial distance (d) from the region of interest (ROI) as illustrated in Figure 2a. The detector thickness (t) has little bearing on the collection solid angle formulae for the discussion which follows, however, it does affect the high energy detection capabilities as discussed elsewhere (Zaluzec, 2009). We also define (Fig. 2b) the detector elevation angle (θ_E) and azimuthal angle (θ_A), which orient the detector relative to the plane normal to the electron beam at the specimen position, and it's rotation relative to the $+X$ translation/tilt axis of the specimen holder. The convention used herein is that θ_E is positive when the detector is measuring signal from the electron entrance surface of an untilted specimen, and θ_A is positive measured from the $+X$ to

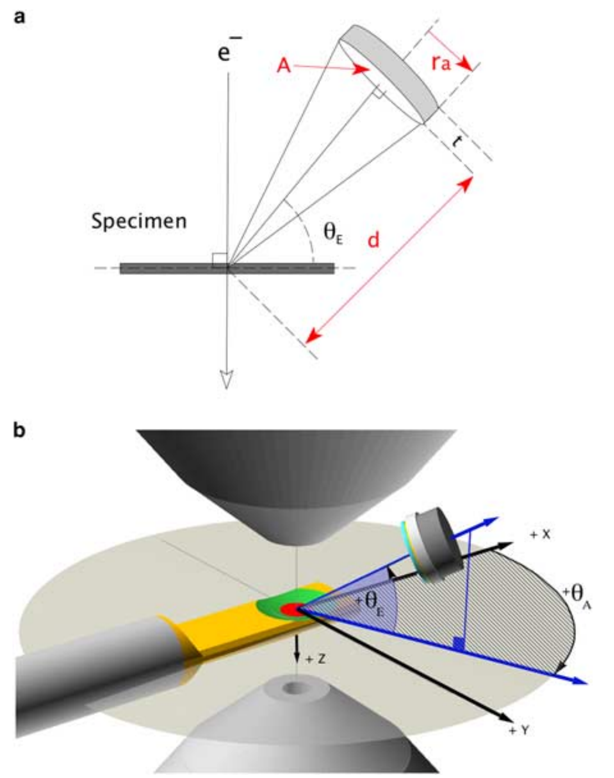

Figure 2. Geometry and parameter definitions for (**a**) circular/cylindrical detector, (**b**) definitions of detector elevation (θ_E) and azimuthal (θ_A) angles.

the $+Y$ specimen holder axis using the standard right hand rule conventions. A value of $\theta_A = 90$ in this coordinate system means the detector is perpendicular to the $+X$ axis of the specimen holder (Fig. 2b). These angles should not be confused with specimen holder tilt angles (θ_x, θ_y).

It is important to note three critical points when using this geometric model to calculate Ω. First, parameter d is the distance to the *active* detector surface from the point of X-ray emission on the specimen and not to the front of any detector mounting/support hardware. Second, r_a is the radius of the *active* area of the detector after accounting for all limiting collimators (Fig. 3a). This radius is generally not the same as the physical radius (r_{physical}) of the detector, which is the parameter that is most often specified by a detector manufacturer. The use of the physical radius over states the detector active area and leads to an overestimate of the solid angle. Depending upon the specific detector design, one must also include, in the determination of r_a, any restrictions introduced by external collimators as well as any internal apertures/rings, which may be integrally mounted to the detector. Such guard rings are installed to improve the signal/background performance of the final device, however, in effect they also reduce the net/active radius. For example, a 30 mm^2 SDD ($r_{\text{physical}} \sim 3.09$ mm) typically has an internally collimated area of 26.4 mm^2 ($r_a \sim 2.9$ mm) (PN Detector, 2013) this difference will have a significant (13%) impact on the calculated value of Ω. Last, it is also essential to account for any ancillary/hidden obstructions between the specimen

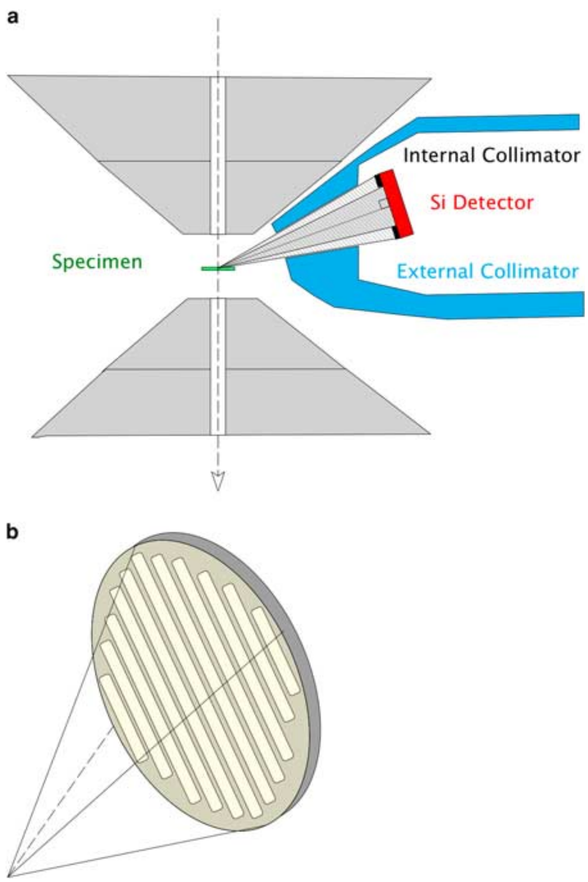

Figure 3. Examples of (**a**) external and internal collimators (blue, black) defining the active area on the detector (red), (**b**) Illustration of a support grid for ultra-thin environmental protection windows having an array of reinforcement/support bars. Such a window, if it is in place, is generally mounted between the external collimator and any internal collimator on the detector.

and the detector surface which can also serve to reduce the net detector active area. In windowless detector configurations this is generally a non-issue, however, in thin or ultra-thin window configurations, an environmental protection window may be reinforced by a physical support grid of significant thickness. This grid (Fig. 3b), which is typically composed of a silicon slotted mesh, blocks ~20% of the active area of the detector (Moxtek, 2013). This reduction in the net area must be included when comparing calculated values of Ω as its effect is an integral part of the detection geometry. To this end, we introduced a pre-factor (f_s), which is the fractional shadowing of the detector by any object or window support grid between the detector active area and the specimen. For an ideal windowless system $f_s = 0$, while for a detector with an environmental window which has a 20% shadowing/support grid $f_s = 0.2$ (Fig. 3b). Consolidating this and referring to the original derivation (Zaluzec, 2009) results in the following equation:

$$\Omega = (1-f_s)\cdot 2\pi \cdot \left[\frac{[r_a^2+d^2-d\cdot\sqrt{r_a^2+d^2}]}{r_a^2+d^2}\right] \qquad (2)$$

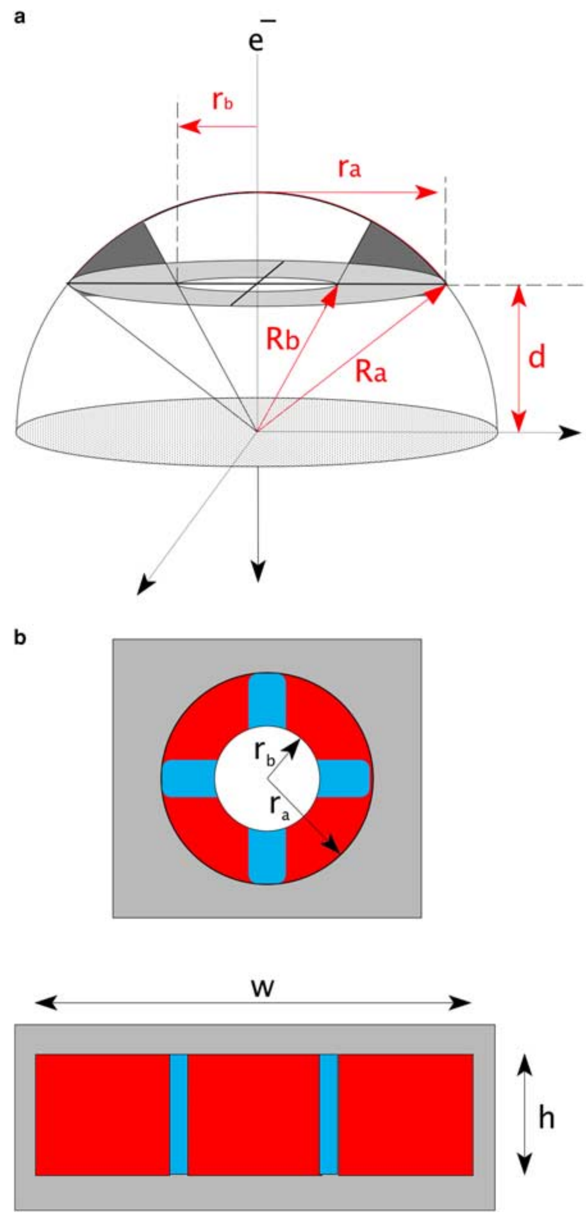

Figure 4. **a**: The geometry of an annular detector whose symmetry axis is collinear with the incident electron beam. **b**: Plan view of annular and rectangular detectors with partial support structures (blue) obstructing and thus reducing the active detector area (red). The grey areas are in-active support structures and thus do not contribute to the detector area.

The maximum theoretical solid angle achievable by a single detector in this geometry is 2π steradians (i.e., 50% of all possible signal), although typical values are significantly lower (~0.2 sr).

Annular Detectors

The annular geometry is schematically illustrated in Figure 4; here the detector consists of an annulus or ring of active area, bounded by outer and inner radii r_a and r_b, respectively. The detector symmetry axis is modeled in this configuration to be collinear with the electron optical axis, with the plane of the detector active area being located a distance (d) above

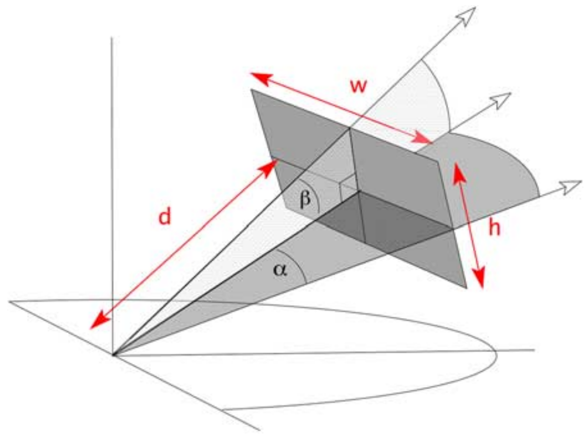

Figure 5. The geometry of a rectangular detector. Note: the surface normal of the rectangular detector in this model is a radial vector to the specimen as in the case of the cylindrical detector. The height (h) and width (w) are of the active area of the sensor and not the physical size of the device.

(or below) the specimen. As in the case of circular cross-section systems, the detector thickness can generally be neglected for this application. f_s has a similar meaning in this geometry, namely the fractional area obstructed by any support structures. An additional caveat for the case of annular detectors is that f_s can also be used to account for any mechanical support structures, which may include structures that physically criss-cross the device to hold components in position (Fig. 4b). Projecting this annular shape onto a sphere yields the following equation:

$$\Omega = (1-f_s)\cdot 2\pi \cdot \left[\frac{\left[r_a^2+d^2-d\cdot\sqrt{r_a^2+d^2}\right]}{r_a^2+d^2} - \frac{\left[r_b^2+d^2-d\cdot\sqrt{r_b^2+d^2}\right]}{r_b^2+d^2}\right] \quad (3)$$

As the inner radius $r_b \to 0$, equation (3) reduces to equation (2). The maximum theoretical solid angle achievable by a single detector in this geometry is similarly 2π steradians. True annular detectors in this shape are seldom constructed. More frequently an array of segmented detectors is located in the form of a ring very closely replicating this geometry (Niculae *et al.*, 2011; PN Detector, 2013).

Rectangular and/or Square Detectors

More recent innovations are detectors having nominally rectangular shaped active areas. The projected surface areas of these detectors can be calculated knowing their active width (w) and height (h) as well as their distance (d) to the ROI. Figure 5 presents this geometry and the resulting solid angle formulae becomes:

$$\Omega = (1-f_s)\cdot 4\cdot \arcsin(\sin\alpha\cdot\sin\beta) \quad (4)$$

$$\beta = \arctan\left(\frac{h}{2d}\right) \quad (5)$$

$$\alpha = \arctan\left(\frac{w}{2d}\right) \quad (6)$$

Square detectors are a subset of the general rectangular case, substituting $h = w$ results in $\alpha = \beta$, and the term in $\sin(\alpha)\sin(\beta)$ is simply replaced by $\sin^2(\alpha)$. As previously discussed, any physical shadowing of the detector area by ancillary windows or support structures is incorporated using the appropriate f_s pre-factor. The maximum theoretical solid angle achievable by this single detector geometry is again 2π steradians. Commercially the corners of these detectors are slightly rounded (PN Detector, 2013) due in part to the presence of internal guard rings as well as fabrication processes, this decrease in area is readily taken into account using the f_s term included in equation (4).

Arrays of Detectors

The use of multiple detectors to increase the effective collection solid angle of an analytical system is not a new concept (Lorimer *et al.*, 1973) and has been implemented successfully by independent researchers as well as commercial manufacturers (Lyman *et al.*, 1994; von Harrach *et al.*, 2009; Argonne National Laboratory, 2010; Tordoff *et al.*, 2012). In the ideal case of non-overlapping independent detectors, the net collection solid angle from an array of detectors is simply the sum of the individual elements, each being calculated separately. For example, Figure 6a illustrates the geometry for a quad array of detectors, which are located symmetrically above and below a specimen in a transmission electron microscope. Although unconventional, X-ray detectors below the specimen have been demonstrated (Zaluzec *et al.*, 1978) and in the past there have been significant problems with this geometry. However, recent measurements have shown that this geometry is now realizable (Zaluzec, 2009*a*, 2014; Argonne National Laboratory, 2010). An alternative hypothetical collection of six detectors rotationally distributed around the electron-optical axis all having a positive elevation angle is illustrated in Figure 6b. Variations of such arrays have been both proposed and constructed (Lyman *et al.*, 1994; von Harrach *et al.*, 2009; Tordoff *et al.*, 2012) to improve the geometrical collection efficiency. However, it is important to recognize that obstruction effects in the limited space in an electron-optical instrument can be substantial. In such a case the net solid angle can decrease due to the mechanical barriers introduced into the line of sight path from the specimen to the detector thus reducing Ω. This topic will be discussed in greater detail in a later section of this paper.

Non-Radial and Elevated Detectors

Equations 1–6 were formulated describing geometries where the detector surface normal is a radial vector to the specimen (as illustrated in Figs. 2a, 2b). While this configuration maximizes the solid angle, for simplicity of construction some detectors are manufactured such that their active area surface normal is perpendicular to the optic axis as illustrated by the geometry sketched in Figure 7a. There are

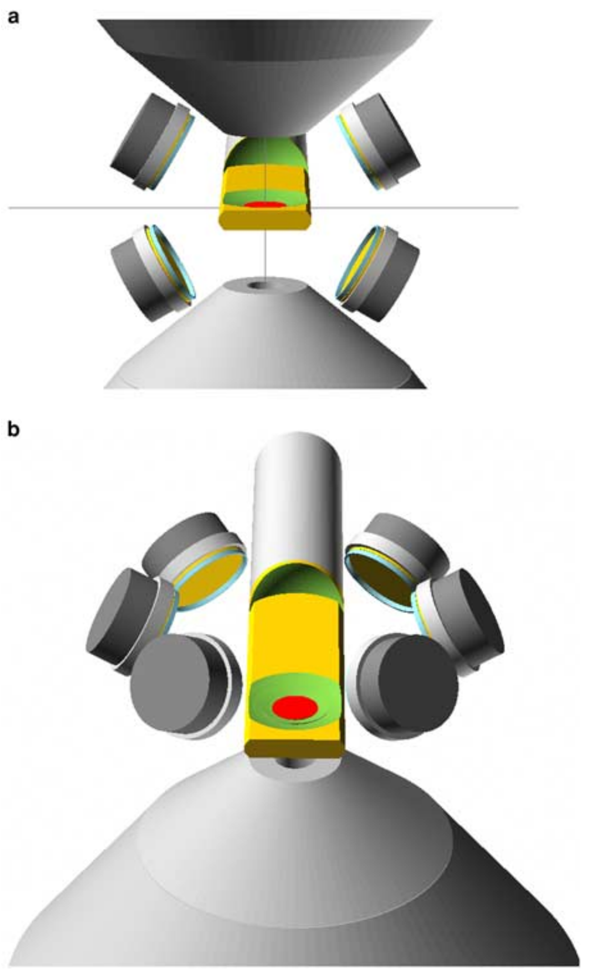

Figure 6. **a**: A quad-array of detectors symmetrically distributed above and below the specimen (red) in an analytical scanning/transmission analytical electron microscopy (S/TEM) geometry (**b**) with an array of six detectors rotationally distributed above the specimen (red).

numerous reasons for this, mostly dealing with ease of construction and interfacing. We will refer to this configuration as the non-radial detector geometry. The effect of this practice on the solid angle is to introduce an effective tilt of the detector when it is projected onto the bounding sphere. This has the effect of foreshortening the areal dimension of a detector along an axis thus decreasing the collection solid angle. This foreshortening causes circular cross-section detectors to have an elliptical projection (Fig. 7b), while rectangular shapes project as thinner rectangles (Fig. 7c). If the non-radially oriented detector's surface normal is perpendicular to the optic axis (as shown in Fig. 7a), then the foreshortening factor can be shown to be equal to a cosine of elevation angle (θ_E) of the detector. This reduces the projected active surface area and necessitates modifications to equations (2–6).

Non-Radial and Elevated Circular Detectors

For the case of non-radial and elevated circular detectors, the resulting elliptical projection, does not have a simple closed

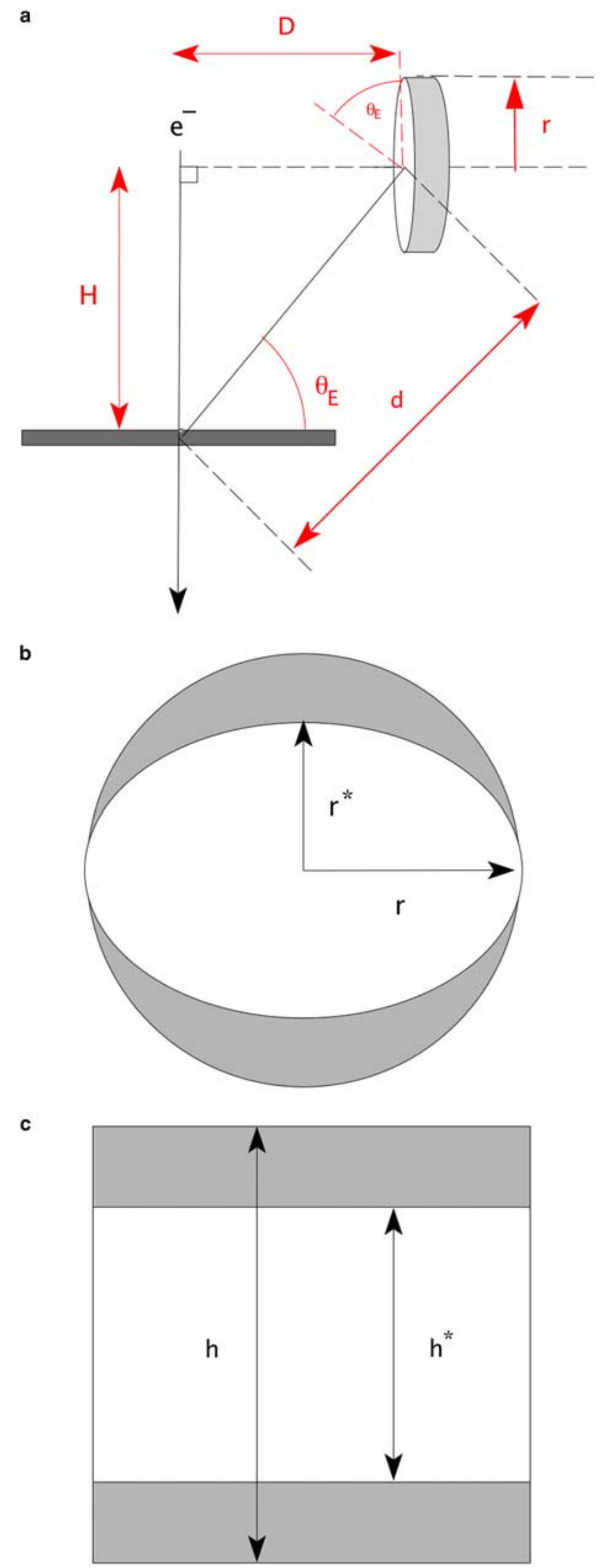

Figure 7. **a**: Illustration of a non-radial detector oriented perpendicular to the optic axis at an elevation angle θ_E. **b, c:** Illustration of foreshortening of the effective detector area for circular (**b**) and rectangular/square (**c**) detectors due in a non-radial detector geometry $r^* = r \cdot \cos(\theta_E)$ and $h^* = h \cdot \cos(\theta_E)$.

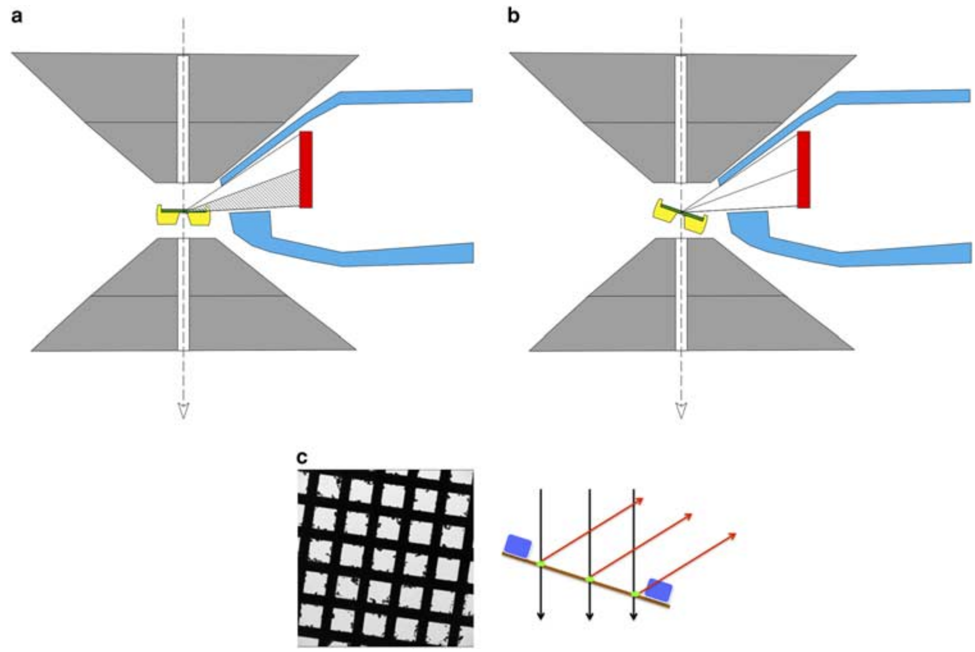

Figure 8. **a**: Cross-section of a scanning/transmission analytical electron microscopy/X-ray energy dispersive spectrometer (S/TEM/XEDS) geometry illustrating the shadowing of the line-of-sight path of a side mounted X-ray detector by the penumbra of the holder (cross-hatched). In this figure the specimen (green) is mounted in the specimen holder (yellow) and is shown untilted (holder tilt $\theta_x = 0$) while the XEDS detector (red) is shown with a positive elevation angle (θ_E). The cross-section is shown through the primary tilt axis of the holder ($\theta_A = 90^o$). **b**: Tilting of the specimen holder ($\theta_X > 0$) to mitigate shadowing of the detector by the holder body allowing the full collection angle to be realized. Note: cutouts on the holder body attempt to minimize this shadow for $\theta_X \sim 0$, but they generally do not completely eliminate it. **c**: Penumbra shadow created by a grid bar (blue) of specimen support film (brown) blocking the line of sight path to the XEDS detector depends upon the relative height of the grid bar and the location of the region of interest (ROI) (green). Here the center and leftmost positions have no restrictions while the rightmost would be severely impacted.

form analytical solution, rather it must be solved using elliptical integrals (Conway, 2010). Defining the elliptical parameters of the non-radial detector as the tuplet (r, r^*) the center of which is still located a distance (d) from the specimen as illustrated in Figs. 7a and 7b, the equation for the subtended solid angle becomes:

$$\Omega = 2\pi - \left[\frac{4 \cdot d \cdot r^{*2}}{r^2 \cdot \sqrt{d^2 + r^2}} \cdot \Pi(\alpha, \kappa)\right] \tag{7}$$

where

$$\kappa = \sqrt{\frac{r^2 - r^{*2}}{d^2 + r^2}} \tag{8}$$

$$\alpha = \sqrt{1 - \frac{r^{*2}}{r^2}} \tag{9}$$

$$r^* = r \cdot \cos(\theta_E) \tag{10}$$

where $\Pi(\alpha, \kappa)$ is the complete elliptic integral of the third kind. Equations 7–10 can be evaluated using any number of modern computer programs (i.e., Mathematica™, Maple™, etc.). As an alternative to the evaluation of the elliptical integrals, we can approximate the decrease in solid angle due to the elliptical projection relative to that of a circle by incorporating a second pre-factor to the formulation developed for the circular geometry. This pre-factor amounts to the ratio of the area of an ellipse of dimensions (r, r^*) to that of a circle of radius r. The ratio of the areal difference is simply related to the ratio of r^*/r. Substituting for r^* from equation 10, one obtains a closed form analytical expression:

$$\Omega = \frac{S}{R^2} = (1 - f_s) \cdot f_{\theta_E} \cdot 2\pi \cdot \left[\frac{\left[r^2 + d^2 - d\sqrt{r^2 + d^2}\right]}{r^2 + d^2}\right] \tag{11}$$

$$f_{\theta_E} = \frac{r^*}{r} = \cos(\theta_E) = \frac{D}{\sqrt{D^2 + H^2}} \tag{12}$$

It should be noted that although this is an approximation it is reasonable for conditions when $\theta_E \lesssim 25°$, a value which is typical of most transmission electron microscopes. For larger detector elevation angles the full elliptical integrals should be employed. As expected as $\theta_E \to 0$ then $f_{\theta E} \to 1$ and equation (11) and equation (2) become identical.

Non-Radial and Elevated Rectangular/Square Detectors

This is the simplest case to consider. For a rectangular detector one simply substitutes for the detector height the relationship $h^* = h\ \cos(\theta_E)$ in equations (4–6) with the remainder being unchanged.

$$\Omega = (1 - f_s) \cdot 4 \cdot \arcsin(\sin\alpha \cdot \sin\beta) \tag{13}$$

$$\beta = \arctan\left(\frac{h \cdot \cos\ (\theta_E)}{2d}\right) \tag{14}$$

$$\alpha = \arctan\left(\frac{w}{2d}\right) \tag{15}$$

The square detector is simply treated as if it were a rectangle, with dimensions $h = h^*$ and $w = h$.

Shadowing of the Detectors

It should be apparent that all of the preceding formulations make an implicit assumption, namely that the ROI of the specimen and the X-rays emitted therefore have a direct line-of-sight path to the detector. This may not always be the case as the line of sight path from the ROI may be partially or completely obstructed by a variety of objects surrounding the ROI on the specimen, the most important of which is usually the penumbra of the body of the sample holder. This shadowing by the body of a holder is illustrated in Figure 8a, which illustrates the most common geometry found in a scanning/transmission analytical electron microscopy (S/TEM) instrument, namely a side mounted single detector which is perpendicular to the primary holder tilt axis ($\theta_A = 90^o$).

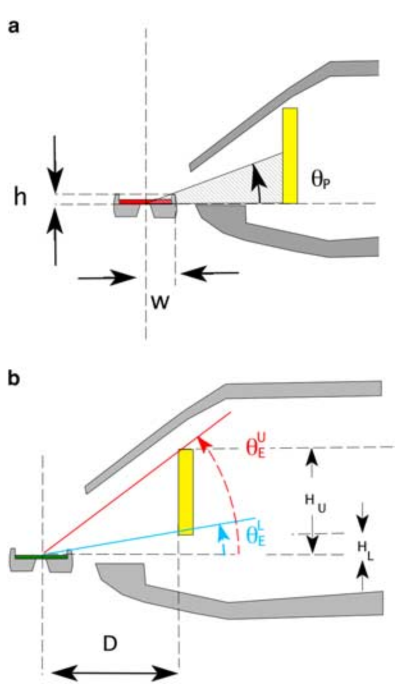

Figure 9. **a**: Calculation parameters of the penumbra angle (θ_P) for shadowing of the detector active area by the specimen holder body. A similar penumbra shadow can also be created by a grid bar supporting a thin carbon or SiN film. **b**: Upper (θ_E^U) and lower (θ_E^L) detector subtending angles.

Should the specimen holder be tilted ($\theta_x > 0$) such that there is no shadowing of the specimen-detector line of sight path (Fig. 8b), then the preceding formulations for collection solid angle directly apply. Using simple geometry, one can readily compute a nominal minimum tilt holder angle (θ_x) which will maximize the collection solid angle by simply noting the relative height of any obstruction and its distance to the ROI. The specifics of the angle will, of course, vary based upon the design of the specimen holder, the position relative to the ROI, the detector elevation angle, and the individual instrument. We should also emphasize that all obstructions in the line-of-sight path to the detector must be accounted for to properly maximize the collection solid angles. While for self-supporting S/TEM specimens (electropolished, ion milled) this obstruction is typically the specimen holder body. For other specimens such as particles on carbon films or focused ion beam liftout specimens, the supporting grid bars and or mounting washers, although physically smaller, may be a more important limiting factor due to their proximity to the region being analyzed (Fig. 8c). With some forethought before an experiment one can calculate a nominal minimum holder tilt angle (θ_x, θ_y) to minimize any shadowing for the various configurations. Referring to Figure 9a, the penumbra angle (θ_P) created, for example, by the specimen holder body (or alternatively a support grid bar) which is of height h and distance w from the ROI is simply:

$$\theta_P = \arctan\left(\frac{h}{w}\right) \tag{16}$$

Numerous detector manufacturers attempt to mitigate the shadowing effect of the specimen holder by mounting the detector at a positive elevation angle (θ_E). The details of the elevation angle differ by vendor and today can vary over the range of 0° to as much as 20° in the S/TEM. Very high elevation angles (~68°) where the detector is located above the upper objective lens pole piece are rarely found in the current generation of instruments due to the extremely long distances (d ~ cm's) which yield vanishing small solid angles (<0.01 sr). In many configurations, as discussed previously, the detector may also be non-radial (Fig. 2a versus Fig. 7a), thus, in addition to knowing the detector elevation and the holder penumbra angles, one must also be cognizant of the subtending angular range of the detector. Not surprisingly, this varies with design and can be strongly influenced by the presence of collimators, as well as the size and distance of the detector from the ROI. To assess this, we define both upper (θ_E^U) and lower (θ_E^L) limits of the subtending solid angle as shown in Figure 7b.

$$\theta_E^U = \arctan\left(\frac{H_u}{D}\right) \tag{17}$$

$$\theta_E^L = \arctan\left(\frac{H_L}{D}\right) \tag{18}$$

At a minimum, in order to maximize the collection solid angle for a specific instrument, one should calculate the

Table 1. Calculated Solid Angles for Various Geometries (Zaluzec, 2013*b*).

Shape	Geometry	Nominal Detector Area (mm^2)	Parameters	Calculated Solid Angle (sr)
Circular	Radial windowless equation 2	30	$A = 26.4\ mm^2$ $d = 12$ mm $\theta_E = 15$ $f_s = 0$	0.176
Circular	Non-radial windowless equation 11	30	$A = 26.4\ mm^2$ $d = 12$ mm $\theta_E = 15$ $f_s = 0$	0.170
Circular	Non-radial supported window equation 11	30	$A = 26.4\ mm^2$ $d = 12$ mm $\theta_E = 15$ $f_s = 0.2$	0.136
Circular	Non-radial windowless equation 11	60	$A = 54.1\ mm^2$ $d = 20$ mm $\theta_E = 10.0$ $f_s = 0$	0.129
Circular	Non-radial windowless equation 11	100	$A = 86.6\ mm^2$ $d = 20$ mm $\theta_E = 10$ $f_s = 0$	0.206
Rectangular	Radial windowless equation 4–6	100	$A = 92.4\ mm^2$ $d = 12$ mm $\theta_E = 10$ $f_s = 0$	0.541
Rectangular	Non-radial windowless equation 13–15	100	$A = 92.4\ mm^2$ $d = 12$ mm $\theta_E = 10$ $f_s = 0$	0.524
Rectangular	Non-radial supported window equation 13–15	100	$A = 92.4\ mm^2$ $d = 12$ mm $\theta_E = 10$ $f_s = 0.2$	0.427
Annular	Radial windowless supported equation 3	60	$A = 54.8\ mm^2$ $r_a = 5$ mm $r_b = 2.75$ mm $d = 5$ mm $f_s = 0.1$	0.956

nominal penumbra angle of the specimen holder and when possible tilt the holder sufficiently to minimize shadowing. A practical starting point would be a holder tilt angle of $\theta_x = \theta_p - \theta_E^L$. A specimen holder tilt of 10–15° is a typical value in modern instruments. We also note that some detector sizes and geometries are such that the detector actually extends below the specimen (Fig. 9b, $H_L < 0$), thus θ_E^L can take on negative values that require even larger holder tilts to mitigate the shadowing effect on Ω. It is also noteworthy to mention that some configurations (i.e., the combination of detector elevation angle and holder design) are such that operation at zero stage tilt is optimal. Examples of this include: the Bruker/PN Sensor on-axis annular detector in a SEM, and the SuperX Quad Detector in the FEI Osiris/ChemiSTEM.

Concluding Remarks

Having compiled this compendium of calculation tools, it is useful to numerically tabulate the application of these formulations to geometries which are encountered in practice in the analytical EM. Thus, in Table 1, we compare radial, non-radial, elevated, circular, rectangular and annular configurations both for windowless detectors as well as detectors having grid-supported windows (Zaluzec, 2013*b*). For the purposes of these calculations we will use various detector elevation angles (0°, 10°, 15°) typical of today's instruments. In all cases the calculations assume that the penumbra of the holder is ≤10° and that the specimen holder is tilted so as to eliminate shadowing. Interestingly, one can see that a 10% loss in solid angle is not uncommon when comparing non-radial to radial configurations, and grid reinforced environmental windows ($f_s \sim 0.2$) have a significant effect. It can also be seen that large area detectors at greater distances do not afford advantages as alluded to in the introduction, while arrays of small close detectors or annular configurations appear to have the greatest merit. Finally while calculations allow one to explore various designs, experimental measurements are certainly more accurate, albeit sometimes more difficult as the parameters needed may not be readily measurable or suitably characterized standard specimens obtainable (Egerton and Cheng, 1994; Zaluzec 2013*a*). It is incumbent upon the researcher to know and/or find reasonable values for the detector parameters for their instrument geometry. Some of these are obtainable from technical drawings of detectors and instruments, which admittedly are sometimes difficult to obtain from manufacturers. Others can be reasonably estimated during installation by careful measurements.

Acknowledgments

This work was supported by the US DoE, Office of Basic Energy Sciences, Contract No. DE-AC02-06CH11357 at the Electron Microscopy Center of Argonne National Laboratory.

References

Argonne National Laboratory. (2010). High collection efficiency X-ray spectrometer system with integrated electron beam stop, electron detector and X-ray detector for use on electron-optical beam lines and microscopes, US Patent 8,314,386, http://www.anl.gov, Argonne, IL, USA.

Conway, J.T. (2010). Analytical solution for the solid angle subtended at any point by an ellipse via a point source radiation vector potential. *Nucl Instr Meth Phys Res* **A 614**, 17–27.

Egerton, R.F. & Cheng, S.C. (1994). Characterization of an analytical electron microscopy with a NiO test specimen. *Ultramicroscopy* **55**, 43–54.

Fitzgerald, R., Keil, K. & Heinrich, K.F.J. (1968). Solid-state energy-dispersion spectrometer for electron-microprobe X-ray analysis. *Science* **159**(3814), 528–530.

Gatti, E. & Rehak, P. (1984). Semiconductor drift chamber – An application of a novel charge transport scheme. *Nucl Instr Meth* **A 225**, 608–614.

Iwanczyk, J.S., Barkan, S., Saveliev, V.D., Tull, C.R., Feng, L., Patt, B. E., Newbury, D.E., Small, J.A. & Zaluzec, N.J. (2005). Large area silicon multi-cathode detector developments for microanalysis and high speed elemental mapping. *Microsc Microanal* **11**(S2), 454–455.

Ketek. (2013). On-line technical specifications. Ketek Product Brochures, München, Germany. Available at http://www.ketek.net

Knoll, G.F. (1999). *Radiation Detection and Measurement*, 3rd ed. chapters 12 and 13. Hoboken, NJ, USA: John Wiley & Sons.

Lorimer, G.W., Razik, N.A. & Cliff, G. (1973). The use of the analytical electron microscope EMMA-4 to study the solute distribution in thin foils: Some applications to metals and minerals. *J Microsc* **99**, 153–164.

Lyman, C.E., Goldstein, J.I., Williams, D.B., Ackland, D.W., Von Harrach, S., Nicholls, A.W. & Statham, P.J. (1994). High-performance X-ray detection in a new analytical electron microscope. *J Microsc* **176**, 85–98.

Moxtek. (2013). On-line technical specifications. Moxtek Product Brochure, Orem, UT, USA. Available at http://www.moxtek.com/x-ray-windows/ap3-ultra-thin-polymer-windows.html

Niculae, A., Bornschlegl, M., Eckhardt, R., Herrmann, J., Jaritschin, O., Lechner, P., Liebel, A., Soltau, H., Schaller, G., Schopper, F. & Strüder, L. (2011). New design and measurements with 60 mm^2 Rococo^2 SDD detectors. *Microsc Microanal* **17**(Suppl 2), 1206–1207.

PN Detector. (2013). On-line technical specifications. PN Detector Product Brochure, München, Germany. Available at http://www.pndetector.de/documents/Brox_spreads_A4-pub.pdf

Soltau, H., Jaratschin, O., Liebl, A., Niculae, A., Smsek, A., Echhard, R., Hermenau, K., Lechner, P., Lutz, G., Schaller, G., Schopper, F. & Struder, L. (2009). New detector architecture for electron microscopes with SDDs. *Microsc Microanal* **15**(S2), 204–205.

Tordoff, B., Beam, S., Schweitzer, M., Hill, E., Kugler, V. & Png, K. (2012). Introducing twin X-ray detectors and fast backscattered electron imaging through a new field emission SEM from Carl Zeiss. Proceedings of EMC-2012, Manchester, September, PS2.2.

von Harrach, H.S., Dona, P., Freitag, B., Soltau, H., Niculae, A. & Rohde, M. (2009). An integrated silicon drift detector system for FEI Schottkey Field Emission Transmission Electron Microscopes. *Microsc Microanal* **15**(S2), 208–209.

Watanabe, M. & Wade, C.A. (2013). Practical measurement of X-ray detection performance of a large solid-angle silicon drift detector in an aberration-corrected STEM. *Microsc Microanal* **19**(Suppl 2), 1264–1265.

Zaluzec, N.J. (1978). Optimizing conditions for X-ray microchemical analysis in analytical electron microscopy. Proceedings of the Ninth International Congress on Electron Microscopy, Toronto, vol. 1, pp. 548–549.

Zaluzec, N.J. (2009*a*). Innovative instrumentation for analysis of nanoparticles: The π steradian detector. *Microscopy Today* **17** (4), 56–59. doi:10.1017/S1551929509000224.

Zaluzec, N.J. (2009*b*). Detector solid angle formulas for use in X-ray energy dispersive spectrometry. *Microsc Microanal* **15**, 93–98.

Zaluzec, N.J. (2013*a*). Direct comparison of X-ray detector solid angles in analytical electron microscopes. *Microsc Microanal* **19** (Suppl 2), 1262–1263.

Zaluzec, N.J. (2013*b*). An on-line web-based program to perform these solid angle calculations is available without charge. Available at http://tpm.amc.anl.gov/NJZTools/NJZTools.html. Accessed December 2013.

Zaluzec, N.J. (2014). XEDS in the AEM: Has everything thing that can be invented, been invented? *Microsc Microanal* **20** (Suppl 2).

Zaluzec, N.J., Kenik, E.A. & Bentley, J. (1978). X-ray microanalysis using an HVEM, *Report of a Specialist Workshop on Analytical Electron Microscopy*, Ithaca, NY, pp. 179–182.